PAPER

Check for updates

Novel AI technology for 4D *in situ* tracking and physicochemical characterization of inorganic carbonaceous aerosols in air/water

Zaki A. Nasreddine, [iD] [a] Devendra Pal [iD] [b] and Parisa A. Ariya [iD] *[ab]

Organic and inorganic aerosol particles in the atmosphere are significant drivers of climate change and pose risks to human health. Biomass burning and combustion processes are substantial sources of these particles, mainly inorganic carbonaceous aerosols (IC) such as black carbon (BC), carbon nanotubes (CNT), and graphite. Despite their environmental relevance, the physicochemical properties of IC are not well characterized, limiting the accuracy of their impact assessments on the Earth's radiative balance and human health. In this study, we demonstrate, for the first time, an *in situ* and real-time quantitative analysis of the physicochemical properties of IC aerosols, including 3D sizes, shapes, phases, and surfaces along with 4D tracking, using an improved nano-digital in-line holography microscope (AI-Nano-DIHM) with a temporal resolution of 62.5 ms. The AI-Nano-DIHM is integrated with two customized AI-driven software programs, enabling automated classification and physicochemical analysis of BC, CNT, and graphite in air and water environments under stationary and dynamic conditions. Our results demonstrate that AI-Nano-DIHM effectively detects nano- and micrometre-sized IC particles, ranging from 60 nm to 200 μm across all three dimensions (width, height, and length). The results obtained from AI-Nano-DIHM were validated using High-Resolution Scanning/Transmission Electron Microscopy (HR-S/TEM) coupled with energy-dispersive X-ray spectroscopy (EDS). We discuss the significant potential of AI-Nano-DIHM as a cost-effective, rapid, and accurate *in situ* and real-time technique for characterizing IC aerosols, with important implications for environmental, and health-related outcomes.

Introduction

Atmospheric aerosols, particularly carbonaceous particles, significantly impact air quality, climate change, and human health.[1–3] These particles, which constitute 20 to 50% of the total aerosol mass,[4] are broadly categorized into two classes: black carbon (BC), primarily composed of elemental carbon (EC),[5] and brown carbon (BrC), which is largely composed of organic carbon (OC).[6] BC originates from a variety of natural and anthropogenic sources, including biomass burning (*e.g.*, wildfires and residential burning), fossil fuel combustion (*e.g.*, vehicular and industrial emissions), and other incomplete combustion processes.[7,8] It directly influences the climate by scattering and absorbing solar radiation,[7] thereby altering the Earth's radiative budget.[9,10] Recent studies highlighted BC's contribution to radiative forcing, which surpasses even that of methane, a potent greenhouse gas.[11,12] Additionally, BC exerts semi-direct effects in the atmosphere, such as the cloud burning effect by favouring cloud evaporation, which further modifies the climate.[13]

BC also influences cloud formation,[14] ice nucleation,[15] regional circulation,[16] and their deposition on snow reduces reflectivity (snow albedo), accelerating snowmelt and contributing to global warming.[17] Despite the environmental and health relevance of BC and other inorganic carbonaceous (IC) aerosols, there remains a critical lack of high-resolution, *in situ*, and real-time data on their physicochemical characteristics, particularly morphology, size distribution, surface roughness, and mixing state.[18] These properties evolve rapidly in the atmosphere due to dynamic processes such as coagulation, condensation, photochemical aging, and mixing with organic compounds like brown carbon (BrC), which can significantly alter the aerosols' radiative forcing through mechanisms such as the lensing effect.[19] Accurate, real-time characterization is essential because the morphology and surface properties of IC particles influence their atmospheric lifetime, optical behavior, cloud-forming potential, and biological interactions.[20] For instance, more irregular or aggregated morphologies can increase light absorption or affect ice nucleation.[21,22] Moreover, particle shape and surface structure directly impact respiratory deposition patterns and toxicity.[23] Thus, understanding these

[a]Department of Chemistry, McGill University, 801 Sherbrooke Street West, Montréal, QC H3A 2K6, Canada. E-mail: parisa.ariya@mcgill.ca

[b]Department of Atmospheric and Oceanic Sciences, McGill University, 805 Sherbrooke Street West, Montreal, QC H3A 0B9, Canada

dynamic physicochemical features in real time is crucial for predicting their environmental and public health effects.[24]

Furthermore, BC particles are associated with adverse health effects. BC, being morphologically at the nanometer size, has been known to transfix into the lungs' deepest regions, facilitating their transportation into the bloodstream.[25] It was also linked to premature death from respiratory infections in addition to a series of health problems such as lung diseases, strokes, heart attacks, bronchitis, and aggravated asthma.[25] The World Health Organization (WHO) has identified BC as a significant risk to public health, especially in regions with high levels of biomass combustion.[26]

Several techniques are used to obtain the physicochemical properties of the emerging IC aerosols. Table S1 (SI) summarizes previous techniques for aerosol characterizations and their limitations. In brief, online methods such as differential mobility analyzers, optical analyzers, and particle sizers[27,28] provide information on particle size and volume distributions yet cannot capture particle shape and morphology. Offline methods, such as impactors and filter sample gravimetric techniques, offer similar information such as size distribution and total mass concentration, similar to some online techniques. However, these methods are subject to particle loss during sample collection, require time-consuming post-processing.[27] These limitations restrict their utilization in capturing the dynamic physicochemical evolution of aerosols under atmospheric conditions.[27,28]

For chemical analysis, online methods like aerosol mass spectrometer[27–29] and Photoacoustic Extinctiometer (PAX)[22,27,30] measure the concentration of BC/aerosols, yet lack information on particle size and their morphological information. Advanced imaging techniques such as Scanning/Transmission Electron Microscopy (S/TEM)[27,31] and Atomic Force Microscopy (AFM),[22,27] provide information on size, phase and morphology but cannot obtain the information in real-time and require samples collection and preparation.[27,28] Techniques such as Fourier Ptychography[22,27,32] and Optical Diffraction Tomography[22,27,33] offer potential for 2D and 3D characterization, however they operate primarily in stationary mode and lack real-time capabilities. Despite significant advancement in BC measurement technologies, there is still a significant gap in determining their physicochemical characteristics, mainly morphology, 2D and 3D size, phase, mixing state (internal and external) and aging in real-time *in situ*.[30,34,35]

This study introduces a novel approach utilizing a fully automated AI-Nano-DIHM for the 4D physicochemical characterization and classification of IC aerosols, including BC, CNT, and graphite, in both air and water environments. The AI-Nano-DIHM enables real-time, *in situ* investigation of IC aerosols' 2D and 3D size, phase, 4D tracking, and surface properties for various sample matrix such as water, molten snow (stationary mode), and air/water (dynamic mode).[22,36,37] Our results provide new insights into the behavior and dynamics of inorganic carbonaceous (IC) aerosols within environmental matrices (Milli-Q water, molten snow, and air), with all findings validated through STEM/EDS.

Methodology

Digital in-line holographic microscopy (DIHM)

DIHM is a type of microscope that enables the observation of particles without the use of a lens.[38,39] It works through a two-stage process.[22] First, a hologram is recorded using the 4deep desktop holographic microscope.[22,40] Second, the hologram is reconstructed using numerical software (Octopus and Stingray Software Package, version 2.2.2).[22] This allows different particles to be visualized and their physicochemical characteristics to be analyzed.[22] The detailed working principle is explained in previous studies.[22,36,37,41,42]

Recording of holograms

As shown in Fig. S1, a laser is emitted from the laser source[22] with a wavelength of 405 nm.[22] The laser passes through a pinhole with a diameter comparable to the wavelength of the laser source.[22] This allows for the light to diffract.[22] The diffracted light hits the object, illuminates it, and eventually produces a significant diffraction pattern (known as a hologram) that is recorded on the screen.[22] The CMOS (complementary metal oxide semiconductor, pixel size 5.5 μm, 2048 × 2048 pixels) photosensitive matrix screen is used to record the hologram.[22,43]

Once the light passing through the pinhole interacts with the object, some portions scatter while others remain unscattered. The term A (r,t) represents the wave amplitude of the hologram recorded on the screen. $A(r, t)$ is given by Eq. (1).[22]

$$A(r, t) = A_{ref}(r, t) + A_{scat}(r, t) \tag{1}$$

$A_{ref}(r, t)$ is the reference amplitude (which didn't hit the object) and $A_{scat}(r, t)$ is the scattered amplitude. The intensity of the recorded hologram is given by eqn (2).

$$I(r, t) = A(r, t)A^*(r, t) \tag{2}$$

$A^*(r, t)$ is the conjugate of the wave amplitude of the hologram at the screen. Expanding the above term gives eqn (3).

$$I(r,t) = A_{ref}(r,t)A^*_{ref}(r,t) + \left[A_{ref}(r,t)A^*_{scat}(r,t) \right. $$
$$\left. + A_{scat}(r,t)A^*_{ref}(r,t) \right] + A_{scat}(r,t)A^*_{scat}(r,t) \tag{3}$$

The first term in the eqn (3) is the intensity of the reference beam.[29] The third term is the intensity of the scattered wave. The second term describes the interference between the reference and the scattered waves, referred as hologram.[22]

Numerical reconstruction

The Octopus and Stingray software is used to numerically reconstruct the hologram.[22] For reconstruction, the required inputs are the distance between the pinhole and the screen, the wavelength of the light, and the camera pixel size.[22] Before reconstruction, a background hologram (captured without any objects) is subtracted from the object-containing hologram to

eliminate optical impurities introduced during the experiment.[22] The Octopus software manually extracts information about the objects' position, orientation, intensity, amplitude, phase, and shape.[22] Stingray software is used to reconstruct the data automatically,[22] and retrieve size, shape and morphology, respectively. Optimal resolution is achieved by manually adjusting the distance 'Z' (the reconstruction position), which represents the distance between the laser source and the reconstructed plane.[44,45] More details about the reconstruction process are explained in previous studies.[22,36,37,41,42]

SMPS and OPS

NanoScan™ SMPS model 3910 (TSI, Inc.) and an OPS model 3330 (TSI, Inc) are used to measure the real-time size distributions of airborne particles.[22] The SMPS measures particle sizes ranging from 10 to 400 nm based on electrical mobility diameter, operating with a sampling flow rate of 0.75 L min^{-1}. The OPS measures particles within a size range of 0.3 to 10 μm, utilizing optical diameter and a sampling flow rate of 1 L min^{-1}.[46]

The purpose of using SMPS/OPS was to independently verify the presence and size distribution of airborne IC aerosols during dynamic mode experiments. These real-time measurements provided number concentration data across a wide size range, confirming that the particles detected by the AI-Nano-DIHM were present in the aerosol flow stream. Although the SMPS/OPS data were not directly integrated into the AI-Nano-DIHM image reconstruction or classification process, they served as important cross-validation tools to ensure the accuracy and consistency of particle detection under real-time and *in situ* conditions. A comprehensive description of the SMPS and OPS methodologies can be found elsewhere.[22,47,48]

Experimental setup

We performed experiments in both stationary and dynamic settings. The stationary mode experiments established a baseline and demonstrated the capability of Nano-DIHM to analyze the morphological and surface properties of IC aerosols in laboratory settings, particularly for samples collected from field or remote regions. In contrast, the dynamic mode experiments enabled the tracking and reconstruction of time-dependent physical properties of BC and other aerosols, providing critical insights into their real-time behavior under atmospheric conditions.[49]

Stationary mode. For stationary mode experiments, the sample was either in powder form or suspended in Milli-Q water or molten snow. First, the microscope slide was cleaned with ethanol or isopropyl alcohol to eliminate dust that could interfere with the experimental setup. The solid sample was retrieved from the bottle using a spatula and placed directly onto the slide. Synthetic IC aerosols were mixed with Milli-Q water by weighing 0.25 g of each solid into 25 mL of Milli-Q water in a conical tube. The tube was then sonicated to apply sound energy, promoting particle agitation and fragmentation to enhance suspension stability.

For molten snow experiments, fresh snow collected from McGill University was placed in a pre-cleaned amber jar (Thermo Fisher Scientific, RRID:SCR_008452) and allowed to melt at room temperature. BC and CNT particles were subsequently spiked into the molten snow, and the spiked sample was transferred onto a clean microscope slide for hologram recording. A background hologram was recorded using unspiked molten snow.

Dynamic mode. For air-phase experimentation, the same samples were aerosolized for dynamic mode experiments. As shown in Fig. S1, the dynamic setup involved a quartz flow tube cuvette (volume: 700 μL; path length: 2 mm), placed on the sampling stage of the AI-Nano-DIHM. Ambient air was directed into the cuvette at a flow rate of 1.7 L min^{-1}, while the outflow at the same rate was routed to the SMPS and OPS for simultaneous particle size analysis. A sevilla C-flow aerosolizer was used to aerosolize either IC suspensions or molten snow samples. These samples were injected into the system using a GenieTouch syringe pump with a liquid feed rate of 0.25 mL min^{-1}. Molten snow was aerosolized to mimic airborne conditions. A detailed description of the setup is provided elsewhere.[22] Fig. S1 shows the experimental setup in stationary and dynamic modes.

3D and 4D characterization of IC aerosols

Octopus software was used for 3D characterization and 4D tracking of IC aerosols. Volume reconstruction was performed on 1000 holograms using Octopus software to retrieve the 3D size distribution and orientation of IC particles. Following reconstruction, both spatial position data (XYZ coordinates) and 3D particle dimensions (length, height, and width) were obtained in real-time and *in situ*.

The procedure for high-resolution trajectory characterization involved the following steps: (a) capturing a sequence of 1000 holograms at a frame rate of 16 fps (temporal resolution: 62.5 ms) using the AI-Nano-DIHM; (b) processing the holograms by saving every two consecutive frames as image pairs, resulting in 500 hologram pairs; (c) subtracting each hologram pair to remove background noise and isolate relevant particle information; and (d) using MATLAB (Version 2022b) to reconstruct and generate a video that visually represents the real-time trajectories of BC particles present in molten snow.[22]

Automation and classification of IC aerosols using the Stingray software

The Stingray software enables the automated processing of thousands of holograms for both offline and online analysis.[22] The process begins to first identify the threshold intensity value, which represents the minimum particle intensity required for object detection.[22] This threshold intensity was determined using Octopus software by performing manual reconstruction. Once the optimal threshold intensity is set, holograms are input into the Stingray software along with recording parameters such as hologram size, camera pixel resolution, laser-to-camera distance, and the threshold intensity value.

The software analyzes the holograms to extract detailed information on the shape, morphology, size, surface area and

edge gradient of particles. Each detected particle is classified into one of the predefined taxa: black carbon (BC), graphite (GC), and carbon nanotubes (CNT) based on their morphological features including intensity threshold, and edge gradient.[42] The classification data is then used to train the IC classifier, which undergoes validation with over 10 000 iterations to achieve accuracy exceeding 95%. This trained classifier is capable of detecting and classifying IC aerosols across different matrices in real-time and *in situ* from unknown samples.

The Stingray software employs a fully automated, AI-based pipeline for real-time classification of inorganic carbonaceous aerosols (IC) such as black carbon (BC), carbon nanotubes (CNT), and graphite. The training process begins by inputting 1000 recorded holograms along with recording parameters including laser wavelength, pixel size, and hologram dimensions. An initial intensity threshold value is optimized based on manually reconstructed holograms to ensure accurate particle detection. Once thresholding is complete, the software automatically detects and isolates particles, extracting morphological and physicochemical properties such as size, edge gradient, surface roughness, perimeter, and surface area. Each particle is then assigned to a predefined taxon (BC, CNT, or graphite) based on these parameters. The classifier is trained through over 10 000 iterations using supervised machine learning techniques to optimize its ability to distinguish among these particle types. After training, the classifier is deployed on unknown samples for real-time, *in situ* detection and classification. Only IC aerosol particles that meet the trained criteria are retained and reported.

The Stingray software can identify particles with a flexibility of ±10% in threshold values.[42] The results include object information such as size, roughness, edge gradient, surface area, and shape. To validate the accuracy, comparisons are made with different types of classifiers, including various aerosols and mixtures.[42] The accuracy of Stingray software may be challenged by complex sample matrices, highlighting the need for a more extensive library to improve detection capabilities for unknown species.[42]

While the AI classifier demonstrates high accuracy (>95%) in controlled laboratory conditions for classifying BC, CNT, and graphite, challenges may arise when applied to complex environmental or heterogeneous samples matrices. Overlapping features between aerosol types, particle aggregates, or non-IC contaminants can challenge the AI's logic, especially in atmospheric samples with high variability. In such cases, untrained or novel particle types may either be misclassified or excluded entirely. Moreover, large datasets may increase computational demand, affecting real-time performance. Future improvements include expanding the training dataset to cover a broader range of aerosol types with varying environmental conditions.

Validation with scanning/transmission electron microscopy HR-S/TEM

The size and morphology of IC particles were validated using high-resolution transmission electron microscopy (HR-S/TEM) coupled with energy-dispersive X-ray spectroscopy (EDS). The same samples used in the AI-Nano-DIHM experiments were also analyzed at the Electron Microscopy Facility of McGill University. For HR-S/TEM imaging, the IC samples were deposited onto copper (Cu) support grids provided by SPI. The samples were examined using an FEI Tecnai G2 F20 HR-S/TEM equipped with a Ceta 16 M 4 k × 4 k CMOS camera and a four-quadrant in-column SDD Super-X detector system. As described previously, EDS was employed to perform elemental analysis of the targeted particles.[22,36,37] The validation results of HR-S/TEM and AI-Nano-DIHM are discussed in Fig. 1 and 2.

Results and discussion

Characterization of BC in aqueous media (snow-borne) and validation by HR-S/TEM

The detection and analysis of black carbon (BC) particles in aqueous samples were performed using the AI-Nano-DIHM system, with results validated by HR-S/TEM (Fig. 1 and 2). These results were validated based on threr main criteria: (i) morphological agreement, including shape and agglomeration patterns of particles (*e.g.*, spherical for BC, tubular for CNT); (ii) dimensional consistency, where sizes measured by AI-Nano-DIHM were within ±10 to15% of those obtained by HR-S/TEM (Fig. 1 and 2); (iii) intensity and phase contrast profiles along particle cross-sections, which reflected internal structure similarly across both methods. The AI-Nano-DIHM successfully retrieved the information on BC particles suspended in water and molten snow (Fig. 1). Fig. 1a shows the hologram recorded with BC particles, and Fig. 1b displays the background hologram without particles. Fig. 1c presents the contrast hologram obtained by subtracting the background from the hologram, effectively removing any extraneous particles originating from the light source or the microscope slide, which is used for the reconstruction to yields the objects' information.[22,42] Fig. 1d provides a zoomed-in view of region (c1), the interest of research, at reconstruction distance $z = 1626$ μm, where multiple BC particles are observed with varying size and morphologies.

Fig. 1e–f depict the intensity reconstruction of BC agglomerates, while Fig. 1g illustrates the phase construction of the same BC agglomerates. Fig. 1i–k present the intensity reconstructions of individual BC particles, and Fig. 1m–p and 1q–t depict intensity and phase crosscuts profiles across the BC particles, respectively. The crosscut profiles reveal that AI-Nano-DIHM detects BC particles of various sizes, ranging from 1 μm to several microns. The sizes obtained by AI-Nano-DIHM are comparable to those obtained by HR-S/TEM when using the same samples, as shown in Fig. 1v.

Both HR-S/TEM and AI-Nano-DIHM produced similar results. They detected sphere-like particles with similar morphologies and sizes. The agglomerates seen in the HR-S/TEM image (Fig. 1u) look very similar to those seen with AI-Nano-DIHM (Fig. 1f). In both cases, the agglomerates had spherical shapes and showed multiple peaks in the intensity profile, which suggests particle clustering. The sizes were also close: the AI-Nano-DIHM showed particles around 5 μm (Fig. 1f), consistent with the HR-S/TEM which showed particles
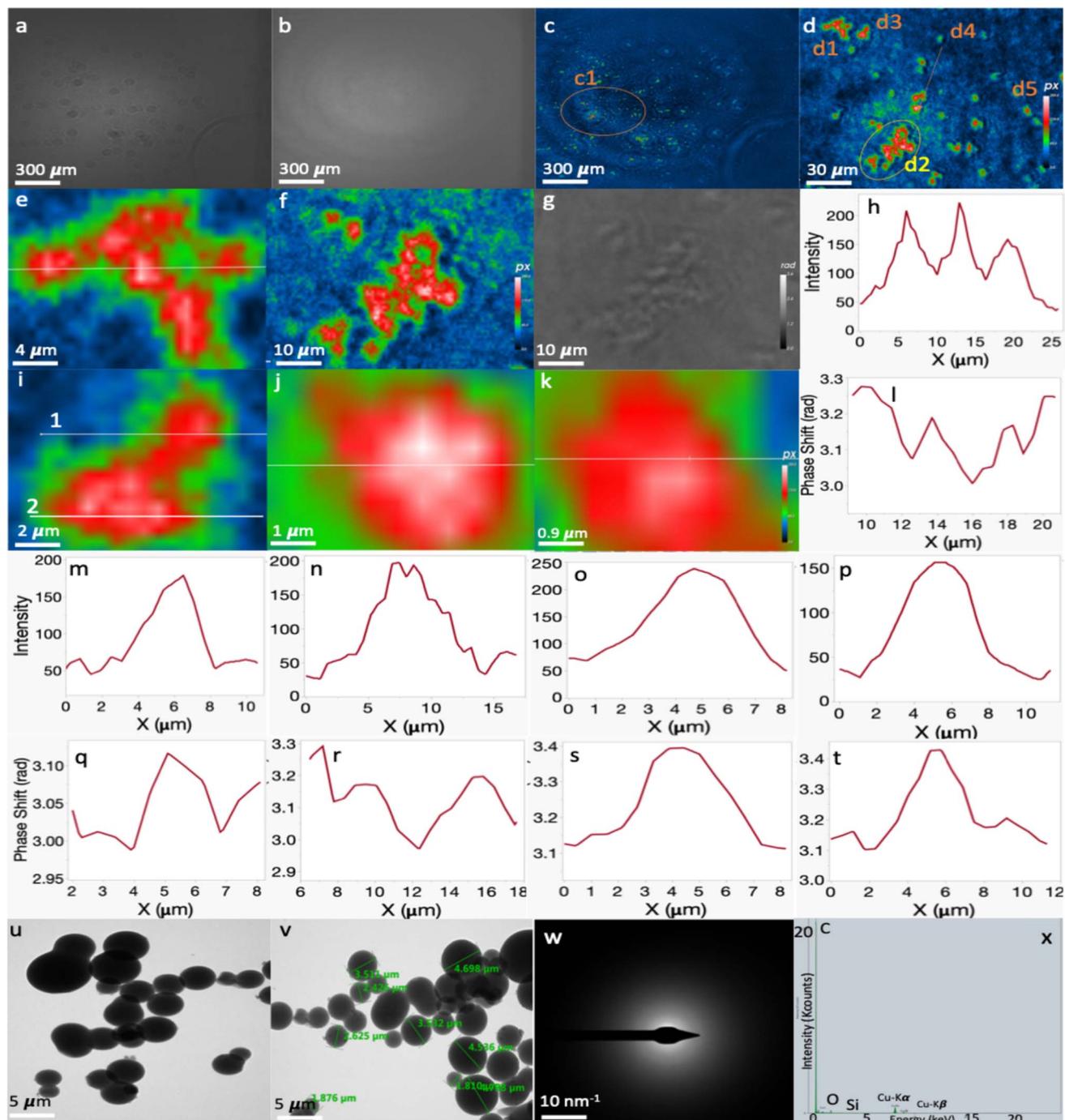
Fig. 1 Reconstruction of the snow-borne BC particles suspended in water and validation with HR-STEM. (a) Raw hologram recorded for BC particles in Milli-Q water; (b) background hologram recorded without BC particles; (c) contrast hologram obtained by subtracting the background hologram from the raw hologram. (d) zoomed-in view of region (c1) showing BC particles in focus at a reconstruction distance of $z = 1626$ μm. (e and f) Intensity reconstructions of BC agglomerates (d1. and d2.) (g) Phase reconstruction of agglomerate d2. (i, j and k) intensity reconstructions of individual BC particles labelled d3, d4, and d5 in panel (d) respectively. The horizontal lines in panels e, i, j, and k shows the crosscut across the BC particles. Crosscuts were selected to represent maximum internal structure. (h, and m−p) Intensity profiles across the crosscuts of d1, d3, d4, and d5. (l and q−t) Phase profiles of d1, d3, d4, and d5 respectively across the particle's crosscuts. (u and v) HR-S/TEM images of similar BC agglomerates and particles. (w) Diffraction pattern, and (x) EDS spectra confirming elemental carbon composition. The AI-Nano-DIHM results exhibit strong agreement in shape, morphology, and size distribution with HR-S/TEM, validating its accuracy.

around 4 μm (Fig. 1v). These findings, supported by visible morphology and multiple peak detection, provide strong evidence to validate the results obtained by the AI-Nano-DIHM.

Fig. 1j and k depict BC particles with spherical shapes like those identified by HR-S/TEM (Fig. 1u and v). The particles exhibit consistent sizes and shapes at similar scales (∼5 μm).
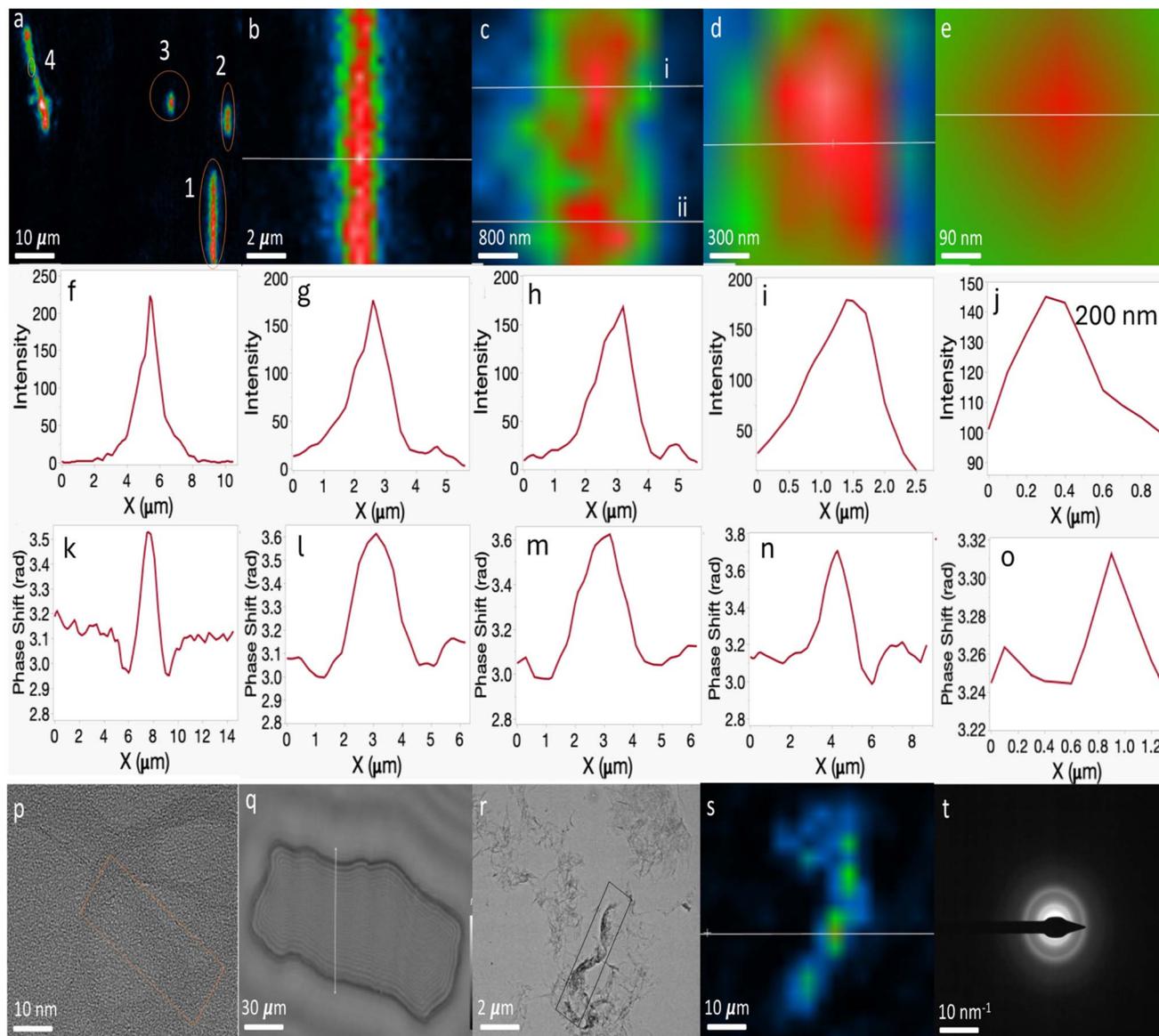
Fig. 2   Reconstruction of carbon nanotube (CNT) particles in Milli-Q water and validation with HR-S/TEM (a) intensity reconstruction of multiple CNT particles (b–e) zoomed-in intensity reconstructions of four CNT particles circled in panel (a). (f–j) Intensity profiles of particles 1–4 across the particles crosscut. (k–o) The phase profiles of particles 1–4 across the particles crosscut. (p–r) HR-S/TEM images of CNT particles showing similar CNT morphology (q) phase reconstruction and (s) intensity reconstruction of a CNT particle. (t) Diffraction pattern. AI-Nano-DIHM successfully captures tubular morphology of CNTs down to 400 nm and aligns with electron microscopy in terms of morphology and size.

While HR-S/TEM detects smaller particles ranging from 1 μm to 5 μm, AI-Nano-DIHM identifies particles from 1.5 to 10 μm. Some larger particles observed by AI-Nano-DIHM may result from two or more particles being separated by distances smaller than the system's lateral resolution, causing them to be identified as a single particle.[22,50] Energy-dispersive X-ray spectroscopy (EDS) analysis confirms that the particles consist solely of carbon. These findings demonstrate the AI-Nano-DIHM's capability to detect individual and agglomerated inorganic carbonaceous aerosols. It is important to note that AI-Nano-DIHM have typically 10% uncertainty from hologram to hologram reconstruction.

Characterization of CNT in aqueous media: Milli-Q water and molten snow (snow-borne) and validation by HR-STEM

Fig. 2 shows the holographic reconstruction of single-walled carbon nanotubes in Milli-Q water and results validated using HR-S/TEM. Fig. 2b–e depict the intensity reconstructions of single-walled carbon nanotubes of varying sizes, while Fig. 2(f–j and k–o) display the intensity and phase profiles across the particles' crosscuts. As observed in Fig. 2, the AI-Nano-DIHM successfully resolves the size and shape of carbon nanotubes down to 400 nm, with particles up to 4 μm in length. Previous research has demonstrated using a holographic microscopy to characterize micron-sized rods, classifying them as nanorods.[51]

The AI-Nano-DIHM successfully captures the shape and morphology of the different carbon nanotube particles, with most carbon nanotubes suspended in Milli-Q water from submicron size to microns sized (Fig. 2). These results are align with findings from Dixon *et al.* (2011),[51] where the 3D distribution of nanorods exhibited a roughly cylindrical volume with a length (L) around 5.0 µm.[51] Comparison with HR-S/TEM shows similar results, depicting shapes and morphologies comparable to those observed with the AI-Nano-DIHM as shown in Fig. 2r and s. The reconstruction results in molten snow are presented in Fig. 3. The AI-Nano-DIHM successfully resolved the size, shape, and morphology of different CNT particles in the snow with nanoscale resolution, as shown in Fig. 3. Fig. 3e–h display various sizes of CNT particles ranging from 5 µm (Fig. 3e) to 900 nm (Fig. 3h). These findings demonstrate the system's ability to detect and characterize inorganic carbonaceous aerosols in Milli-Q water and snow. Table 1 shows comparison of AI-Nano-DIHM and HR-S/TEM validation results.

Another objective was to showcase the AI-Nano-DIHM's capability to distinguish between other various carbonaceous aerosols within the same family (IC aerosols). For this, graphitic carbon aerosol particles were analyzed. The results for graphite

in Milli-Q water are shown in Fig. S2, while graphite in powder form is depicted in Fig. S3. AI-Nano-DIHM effectively resolves graphite particle size ranges from 900 nm to 1000 nm.

Fig. S2a and b show the agglomeration of two graphite particles forming one single particle beyond the lateral resolution of AI-Nano-DIHM. The crosscuts in Fig. S2d and e reveal sizes of 2.6 µm and 5.2 µm, respectively. This discrepancy confirms that Fig. S2a does not depict a single particle but rather an agglomeration of two particles or a graphite particle with an impurity, likely due to carbonaceous aerosol mixing in the atmosphere.[52]

Airborne IC aerosol detection: insights into particle dynamics

The AI-Nano-DIHM system also tested for charactrisation of airborne particles which is important for investigating their behavior in the atmosphere. The experimental procedure follows the detailed methodology outlined in previous work[42] and is briefly explained in the method section.

Fig. 4 presents the reconstruction of airborne BC particles, while Fig. 5 shows the reconstruction of airborne CNT particles. BC particles appeared spherical; CNTs exhibited circular, elongated shapes due to the aerosolizing of CNT particles[22]
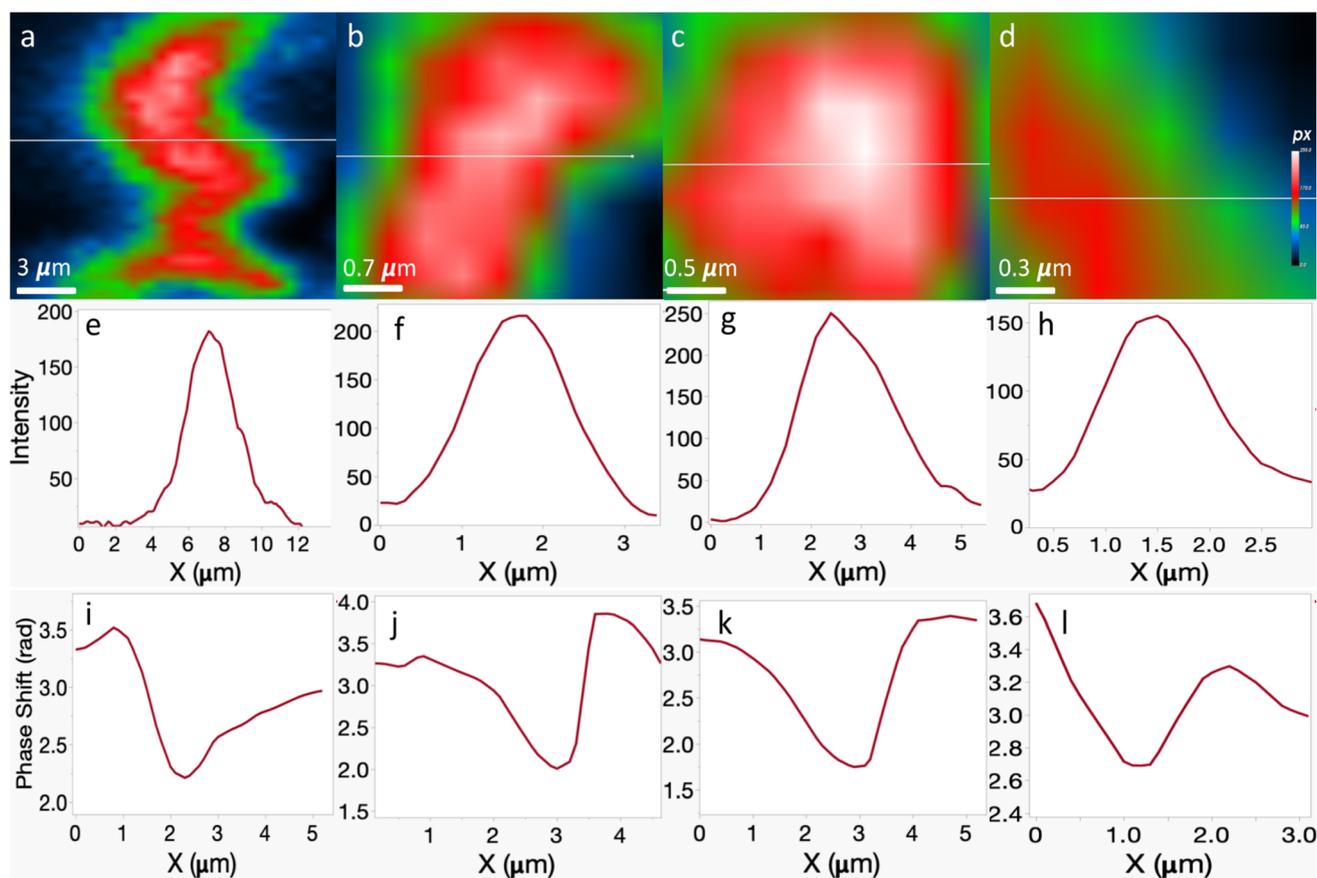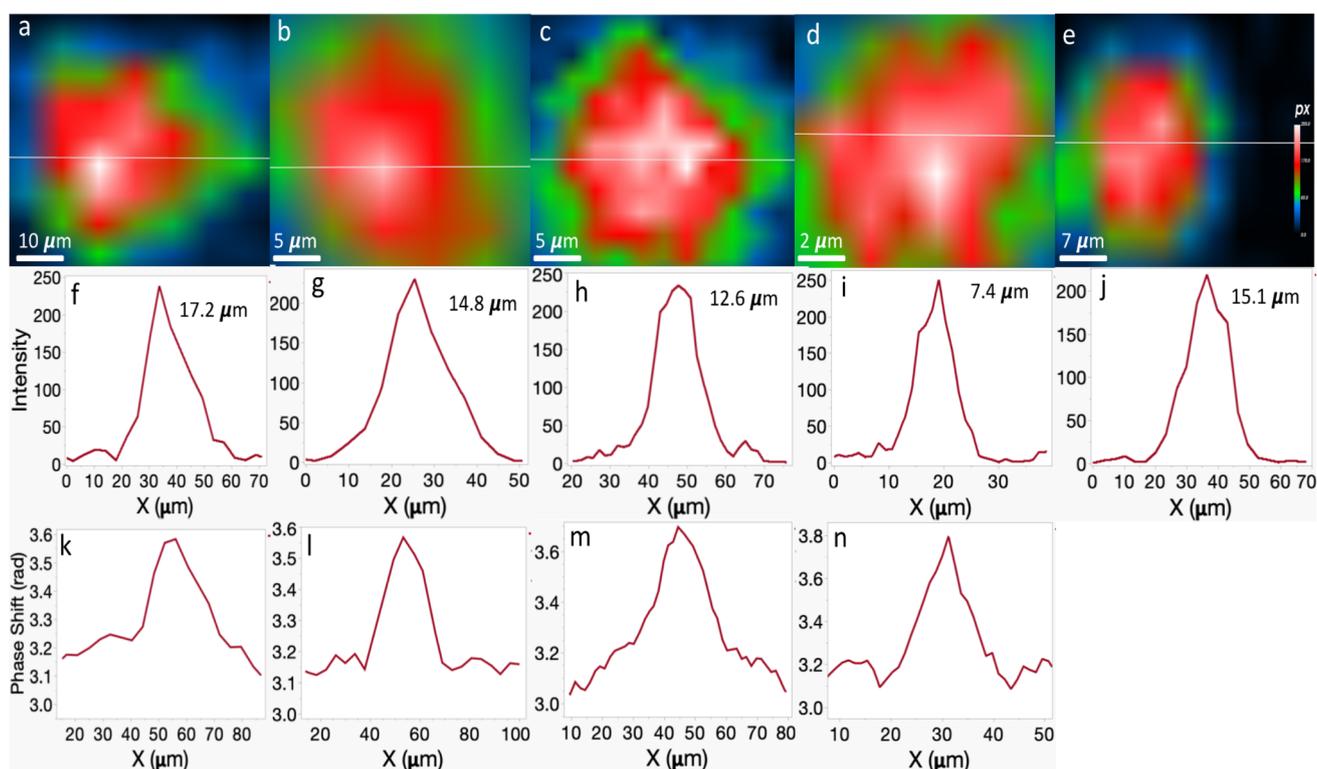

Fig. 3 AI-Nano-DIHM reconstruction of CNT particles detected in molten snow. (a–d) Intensity reconstructions of different CNT particles in focus at a reconstruction distance of $z = 400$ µm, (e–h) show the intensity profiles through the particles' crosscuts, revealing tubular shape and submicron features. (i–l) Corresponding phase profiles across the particles' crosscuts. These results demonstrate the system's ability to resolve nano/micrometer-scale tubular particles in complex aqueous matrices such as snow.

Table 1 Comparative summary of AI-Nano-DIHM and HR-S/TEM validation results for different inorganic carbonaceous (IC) aerosols. This table presents a side-by-side comparison of observations obtained using AI-Nano-DIHM and HR-S/TEM for black carbon (BC), carbon nanotubes (CNT). Consistent results across both techniques confirm the reliability of AI-Nano-DIHM for real-time, *in situ* characterization of IC aerosols

Aerosol type	Matrix	AI-Nano-DIHM observations	HR-S/TEM observations	Validation agreement
Black carbon (BC)	Milli-Q water/snow	Spherical/agglomerated morphology; size range: 1–10 μm; multiple peaks in intensity and phase profiles	Spherical/agglomerated morphology; size range: 1–5 μm; high resolution	Strong agreement in size, morphology, clustering
Carbon nanotubes (CNT)	Milli-Q water/snow	Tubular structures; size range: 0.4–4 μm with submicron-micron tubular particles; cylindrical profiles	Tubular; size range: 0.5–5 μm with similar dimensions and shape; consistent with reconstructed features	Good agreement in length, shape, and alignment

Fig. 4 Reconstruction of airborne BC particles using AI-Nano-DIHM: (a–e) Intensity reconstruction of distinct BC particles captured in the air phase. (f–j) Intensity profiles through the particles' crosscuts, (k–n) show the phase profiles through the particles' crosscuts. Note that the phase profile of particle (e) could not be detected. Results confirm the AI-Nano-DIHM's ability to resolve airborne BC particles with submicron–micron resolution in real time.

while in CNT exhibited elongated tabular morphology in stationary mode (Fig. 2).

The 3D reconstruction of BC and CNT particles is shown in Fig. 6. Fig. 6a and c illustrate the orientation of BC and CNT particles, respectively, while Fig. 6b and d display the 3D size distribution (width, height, length) of BC and CNT particles. The statistical analysis in Fig. 6e shows that the first percentile values for BC particle dimensions are 60 nm (width), 60 nm (height), and 950 nm (length), while CNT dimensions are 70 nm (width), 100 nm (height), and 2.02 μm (length). These results demonstrate AI-Nano-DIHM's ability to detect submicron and nano-sized IC particles. The predominantly elongated shape of

BC particles can be attributed to the agglomeration of ultrafine BC particles which result in its elongated form.[53] Van der waals forces and electrostatic/hydrophobic interactions favor the formation of such structures. The reason behind the predominant agglomeration along the length dimension is attributed to the anisotropic nature of BC particles which minimizes energy unlike agglomeration along other dimensions (width or height) which would add strain on the agglomerate rendering it unstable.[54] Another reason could be due to the limitation of AI-Nano-DIHM depth resolution.[22]

AI-Nano-DIHM results clearly demonstrate its potential for real-time and *in situ* monitoring of IC aerosols in the air. The
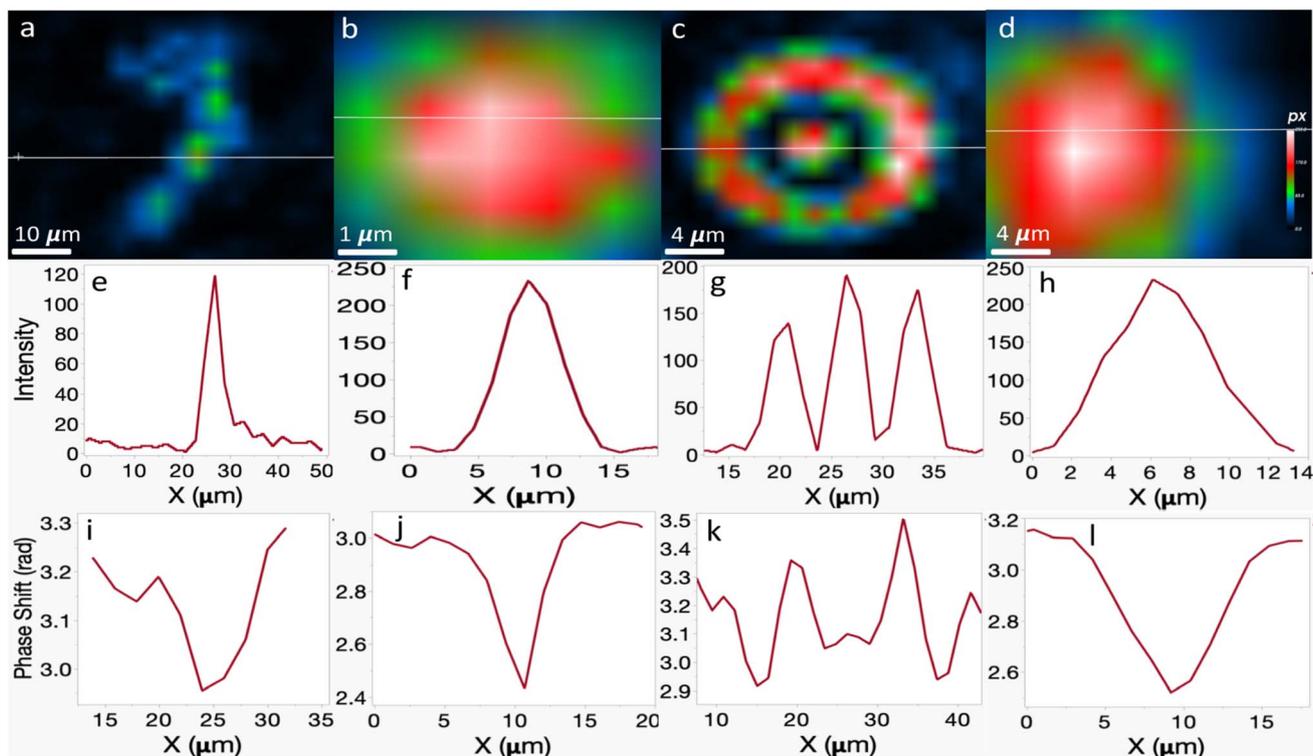
Fig. 5 Reconstruction of airborne CNT particles: (a–d) Intensity reconstructions of different airborne CNT particles, showing circular to elongated morphologies. (e–h) Intensity profiles through the particles' crosscuts, and (i–l) show the phase profiles through the particles' crosscuts. Differences from stationary CNT morphology (Fig. 2) reflect deformation during aerosolization. AI-Nano-DIHM successfully captures airborne CNTs in dynamic environments.

technology provides valuable insights into the size and shape of BC and CNT particles in the atmosphere, thus amplifying our understanding of their effects on environmental dynamics.

4D tracking of BC in molten snow: environmental implications

Fig. 7 displays selected frames from a time-resolved sequence illustrating the 4D (3D + time) monitoring of BC particles in molten snow samples. Tracking BC particles within snow is particularly interesting due to their potential migration vertically and horizontally within the snowpack and thus impact on snowmelt and albedo.[55] The video shows how BC particles move randomly, horizontally, and vertically, without following a specific trajectory[29] suggesting that the BC deposition on snow surfaces could downwards to snow depth and surfaces. Aerosols particles are known to have random motion, and the trajectory exactly captures the random path.[56] Even if sample flow was more predominant in *XY* direction, but particles were all over the place. This behavior has important implications: deeper embedded BC can continue to absorb solar radiation, enhancing localized heating and meltwater percolation.[57] The capacity of tracking particles provides valuable insights into the behaviour and dynamics of BC particles within the snow, enhancing our understanding of their interactions and distribution in this environment.
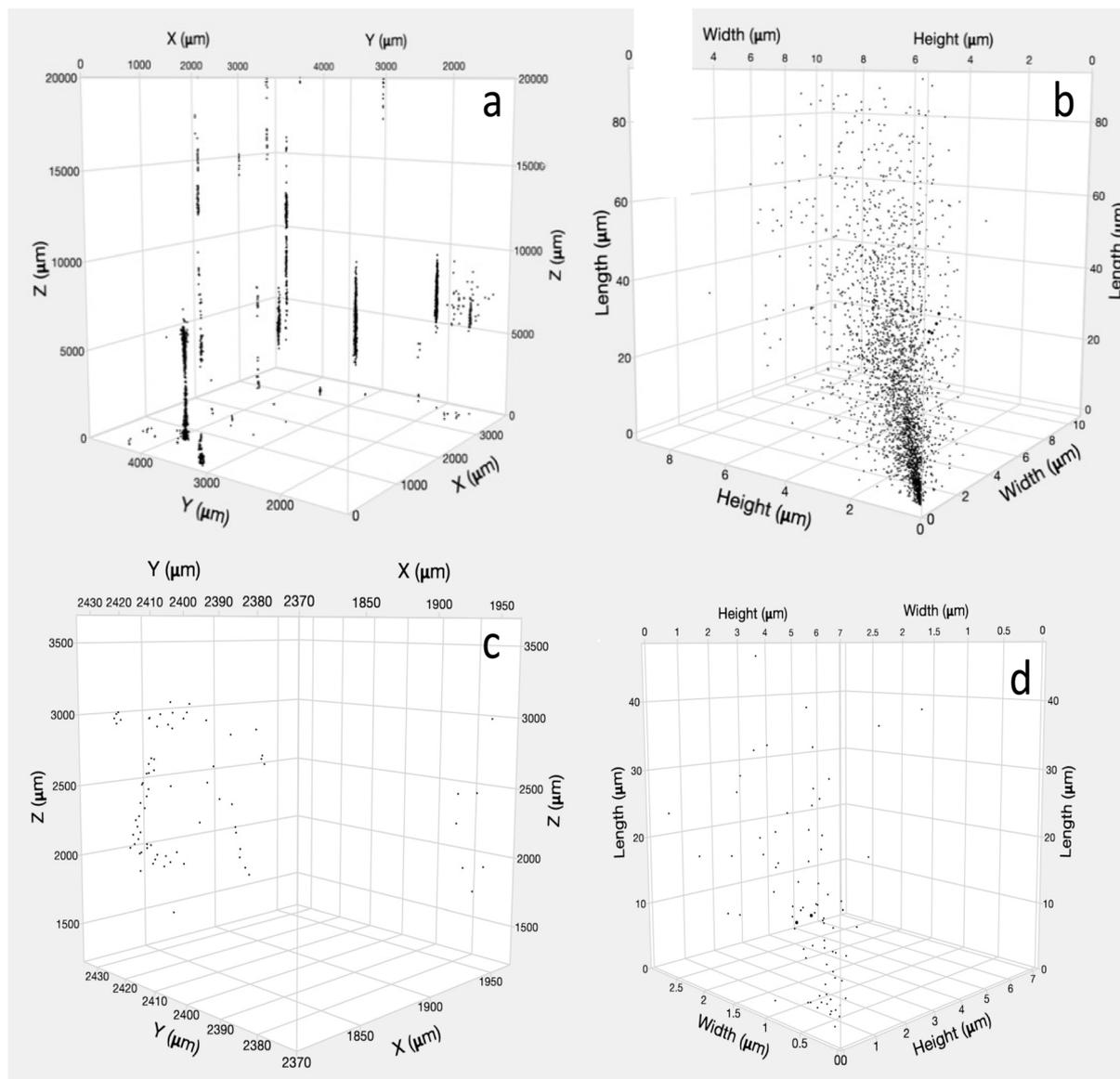
Although it is not a focus of the study, the real-time tracking data obtained from AI-Nano-DIHM can be used to calculate

particle velocity and trajectory, which could be influenced by environmental factors such as temperature, water content, and snow structure.[36] The AI-Nano-DIHM's ability to track these particles with high temporal and spatial resolution offers a powerful tool for studying the impact of BC on air-cryosphere/water processes.

Automation and classification of inorganic carbonaceous aerosols

The Stingray software was trained to classify and detect the real-time, *in situ* physicochemical characterization of several IC aerosols, including BC, CNT, and graphite, in several sample media (powder form, Milli-Q water, molten snow, and air). The training involved more than 1000 holograms and 10 000 iterations to optimize accuracy. Surface roughness (R_a) was computed as the mean deviation from the central plane across the particle surface.[58] Specifically, the Stingray software uses internal algorithms based on Kirchhoff–Fresnel reconstruction[22] approach to quantify roughness by analyzing fluctuations in edge intensity gradients obtained from contrast-based phase retrieval of each hologram.[58] The resulting roughness index is derived from the standard deviation of these phase/intensity variations, normalized to particle size. While not equivalent to nanometric topography obtained using AFM, this optical roughness metric provides a indicator of morphological texture, useful for distinguishing between particle types such as smooth, spherical BC and layered or fibrous structures like

e	BC			CNT		
	Width (µm)	Height (µm)	Length (µm)	Width (µm)	Height (µm)	Length (µm)
Mean	1.51	1.46	23.30	0.97	0.91	15.84
Median	1.22	1.17	18.40	0.67	0.72	13.70
Standard Deviation	1.24	1.21	16.81	0.99	0.72	10.57
1st Percentile	0.06	0.06	0.95	0.07	0.10	2.02
99th Percentile	4.93	5.01	66.71	3.62	2.93	45.82

Fig. 6 3D Reconstruction and statistical analysis of airborne BC and CNT particles. (a and c) Particle orientation, and spatial distribution of airborne BC and CNT particles respectively. (b and d) Distribution of particles' length, height and width retrieved from 3D reconstruction (e) summary table showing statistical parameters of BC and CNT for each dimension. The data illustrate the submicron to tens-of-micron scale range of IC aerosols and confirm AI-Nano-DIHM's capacity to retrieve size metrics in 3D.
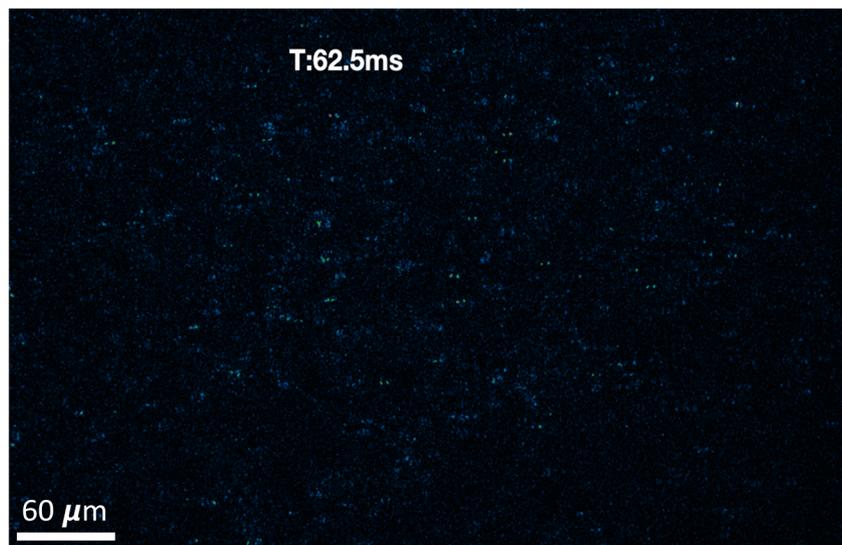
Fig. 7 4D tracking of BC particles in molten snow. Selected sequential frames extracted from a 1000-frame holographic video series showing real-time (3D + time) trajectories of BC particles in molten snow. Particle motion is random and multidirectional, revealing complex dynamics in snow matrices. These trajectories offer insights into the behavior of embedded BC and its implications for snow albedo and melt processes.

graphite and CNTs. A detailed discussion of the automation process is provided in the methodology and previous publications.[22,36,37,41,42] Table 2 presents the automated detection and classification of IC aerosols using the Stingray software and the corresponding physicochemical properties (morphological properties, 2D and 3D sizes) of IC aerosols. For instance, CNT particles exhibited higher area and perimeter values than BC and graphite. It can be understood because CNT particles have more tabular morphology than compared to spherical BC particles. Graphite particles showed more significant surface roughness and edge gradients, reflecting a complex surface variability. The main possible reason of this would be attributed to graphite's layered 2D structure unlike other IC aerosols, which could lead to surface defects and irregularities, thus exhibiting more significant surface roughness and edge gradients.[59] This capability is particularly valuable when analyzing unknown samples. By analysing unknown sample through the automated AI-Nano-DIHM and selecting the trained classifier for IC aerosols, the AI-Nano-DIHM can automatically classify and detect the presence of IC aerosols in the sample. This demonstrates the potential of the AI-Nano-DIHM system for real-time, *in situ* detection and characterization of IC aerosols across different media.

Comparison between IC aerosols in solid form and in aqueous form

Solid samples (powders) show noticeable differences from aqueous samples (Fig. S2 and S4–S6). The powders primarily exhibit agglomerates of BC particles with varying sizes. These aggregates are likely formed due to van der Waals forces between particles. In contrast, samples in Milli-Q water show a more dispersed distribution of BC particles, often forming colloidal suspensions. This dispersion is attributed to the

sonication process, during which sound energy breaks down the agglomerates.

Analyzing the cross-sectional reconstructions, we observe that dispersing black carbon (BC) particles in Milli-Q water modifies their optical properties. This change is attributed to interactions between BC particles and the surrounding medium. In powder form, BC tends to agglomerate, leading to increased light scattering and reduced accuracy in optical characterization. These findings highlight the influence of the surrounding medium on the behavior of carbonaceous aerosols. Fig. S3 presents the holographic reconstruction of graphite particles, while Fig. S4 shows the corresponding reconstruction of BC particles in powder form.

Fig. S5 and S6 illustrate single-walled CNT particles in powder form. Carbon nanotubes (CNT) appear with rectangular shapes. The crosscuts reveal that this shape results from the agglomeration of individual CNT particles. These rectangular shapes are attributed to bundles of individual CNTs stacked horizontally, forming the observed morphology. Fig. S6a in the supporting information supports this claim. As depicted, the vertical crosscut reveals the presence of multiple peaks, which could be attributed to multiple CNT tubes. Had it been a single CNT, the crosscut would show a single peak, as shown in Fig. S5a. This confirms that several single CNTs stack over each other horizontally, forming the observed rectangular morphology. The AI-Nano-DIHM reveals how carbonaceous aerosols behave differently in various media.

CNT particles tend to agglomerate in powder form, highlighting distinct physicochemical characteristics within the agglomerates. In Milli-Q water, the AI-Nano-DIHM detects the dispersion of individual CNT particles. While the powder form exhibits a variety of morphologies among CNT particles (curved, straight, *etc.*), Milli-Q water reveals a consistent morphology: straight cylindrical tube structures. This observation

Table 2 Automated detection and classification of three types of IC aerosols: BC, CNT, and graphite using Stingray software. The table presents physicochemical parameters of individual IC particles detected in various sample media (powder, Milli-Q water, molten snow, and air). Parameters include 3D spatial coordinates (X, Y, Z), particle dimensions (length, width), 2D area, perimeter, edge gradient, and surface roughness. CNT particles exhibit larger area and perimeter due to their elongated, tubular morphology. Graphite particles show higher surface roughness and edge gradient, likely due to their layered and irregular sheet structure. These features demonstrate the capability of the AI-Nano-DIHM system to distinguish between aerosol types based on morphological signatures in real-time and *in situ*
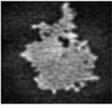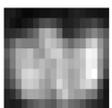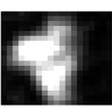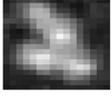
Taxon	Image	X (µm)	Y (µm)	Z (µm)	Length (µm)	Width (µm)	Area (µm²)	Perimeter (µm)	Edge gradient	Roughness
BC		618.19	677.64	3228.73	95.11	62.13	3673.97	310.76	32.55	1.290
		440.64	343.69	2598.98	19.27	16.16	132.48	70.60	31.32	1.319
		379.02	618.12	2592.79	54.12	25.10	696.71	199.28	40.00	1.655
		934.63	222.43	3516.71	23.49	12.43	214.73	61.20	49.40	1.042
		135.27	185.73	936.92	6.64	4.54	23.60	19.19	38.67	1.039
		295.37	289.52	2575.99	9.86	8.01	44.59	28.68	33.25	1.082
CNT		263.04	300.73	910.87	232.65	83.08	15 136	572.63	26.84	1.125
		142.91	183.06	467.38	174.11	127.51	14 870.40	947.84	21.79	2.269
		1611.62	1333.31	17 463.12	592.13	313.91	115 008	1537.30	28.08	1.180
		114.93	159.60	372.30	25.73	2.83	37.79	54.95	23.32	1.114
Graphite		529.12	492.80	2158	2.85	1.90	3.62	7.86	105.24	1.001
		802.21	497.39	1597	23.95	12.62	199.78	65.69	68.24	1.222
		447.11	675.29	2730.79	25.31	18.56	292.31	69.16	30.73	1.106
		850.55	731.26	2912.78	72.84	69.21	2468.54	313.22	30.30	1.441
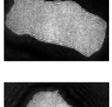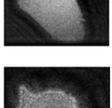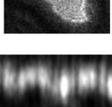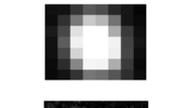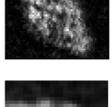
Table 2 (*Contd.*)

Taxon	Image	X (μm)	Y (μm)	Z (μm)	Length (μm)	Width (μm)	Area (μm²)	Perimeter (μm)	Edge gradient	Roughness
		228.66	328.19	2295.85	40.70	13.76	433.69	93.51	24.89	1.057
		497.27	493.73	2158	3.32	2.37	4.62	8.81	58.99	1.011

underscores the influence of the surrounding medium on the behavior and morphology of carbonaceous aerosols. Like other carbonaceous aerosols, the AI-Nano-DIHM distinguishes between graphite powder aerosols and those dispersed in Milli-Q water.

Comparing the results reveals a consistent trend: particles in powder form appear as agglomerates of different individual particles, while those in Milli-Q water are dispersed, allowing for the visualization and study of individual aerosol particles. This distinction is reflected in the crosscuts, where powder particles exhibit multiple peaks, indicating condensed aggregation. In contrast, aerosols in Milli-Q water display a single peak, indicating the presence of a single particle.

AI-Nano-DIHM: limitations and future insights

While AI-based particle recognition has been increasingly applied in platforms such as AFM and SEM, these methods typically require vacuum or contact conditions, are limited to static samples and cannot detect airborne particles in real-time and *in situ*.[60] In contrast, the AI-Nano-DIHM system used in this study enables real time, *in situ* analysis of aerosol particles in both aqueous and airborne media, without the need for sample drying, coating, or immobilization.[22] Unlike AFM/SEM-based systems that analyze static images post-acquisition, Stingray software performs rapid analysis of thousands of holograms per second, extracting morphological parameters (*e.g.*, edge gradient, roughness, and 3D sizes). Additionally, the AI-Nano-DIHM allows for 3D and 4D characterization,[22] both of which conventional AI techniques can not achieve.[22] These features make the system uniquely suited for atmospheric and environmental studies, where particle dynamics, phase, and mixing state are critical.

AI-Nano-DIHM, while highly effective for detecting and analyzing particles in the nano-to micrometer size range, faces several limitations. It is limited to detect submicron and micrometer-size particles, with difficulties arising when measuring particles smaller than 60 nm unlike HR-S/TEM and

AFM.[61] Overcoming the diffraction limit for such small particles has been an area of ongoing research. However, unlike conventional methods (Table S1), AI-Nano-DIHM does not require sample drying, coating, or preparation, and captures data in dynamic conditions, preserving the native state of aerosols. In contrast, offline methods offer superior elemental or atomic-scale imaging but at the cost of temporal resolution (Table S1). Additionally, the system also struggles with achieving high spatial resolution, particularly when attempting to resolve individual nanoscale particles within aggregates.[22] This limitation is further compounded by challenges in complex or heterogeneous environments, where overlapping aerosol types or complex matrices can reduce the accuracy of particle classification. Using more complex environmental samples (*e.g.*, wildfire plumes, urban smog) will require further testing and calibration under varying atmospheric conditions along with enhanced computational processing, and integration with portable sampling systems. Our future ongoing work focuses to address these challanges by improving depth resolution, expanding particle classifiers, and validating AI-Nano-DIHM performance in ambient field conditions. Despite these limitations, the AI-Nano-DIHM offers unique advantages in real-time IC aerosol monitoring across multiple media, supporting advances in environmental sensing and health impact assessments.

Conclusion

This study demonstrates the capability of AI-Nano-DIHM for *in situ*, real-time characterization of three types of inorganic carbonaceous (IC) aerosols, including black carbon (BC), carbon nanotubes (CNT), and graphite in different environmental media. The AI-Nano-DIHM effectively captures and reconstructs the hologram images and retrieves detailed physicochemical information on IC particle morphology, size distribution, and surface properties in air and aqueous environments. BC particles were predominantly spherical, with sizes ranging from 1 to 10 μm, while CNT particles exhibited cylindrical tube-like structures, lengths between 400 nm and 4

μm. Graphite particles were found to have rectangular sheet-like structures with lateral dimensions up to 5 μm. The AI-Nano-DIHM system's accuracy was validated through HR-S/TEM comparisons, which confirmed similar morphologies and size distributions across all three aerosol types.

Moreover, the AI-Nano-DIHM system's capabilities extend beyond characterization. It enables dynamic tracking of BC and CNT particles in air, providing valuable insights into their atmospheric behavior. The 4D tracking (3D + time) of BC particles in snow revealed random motion, highlighting the system's potential for studying BC's role in snowmelt and albedo modification.

Many researchers have noted the increasing number and intensity of forest fires worldwide, leading to the creation of black and brown carbons.[62] This study underscores the significant potential of AI-Nano-DIHM as a robust tool for the real-time, *in situ* detection and characterization of inorganic carbonaceous aerosols like black carbon, carbon nanotubes, and graphite. Further work is recommended to expand its use to more complex aerosol mixtures and environmental conditions.

Author contributions

Z. N. and D. P. designed and performed the experiments. Z. N. performed the data analysis, drafted and wrote the manuscript. D. P. contributed to data analysis, wrote, and revised the manuscript. P. A. A. conceived this project, wrote the funded proposal, which provides the basis of this work, and supervised Z. N. and D. P., and revised the manuscript.

Conflicts of interest

The are no conflicts to declare.

Data availability

All the numerical data generated in this study are available within the paper in graphical representation. The data that support the findings of this study are available from the corresponding author upon reasonable request. The data supporting this article have been included as part of the SI. Fig S1. (a) Stationary mode setup, (b) dynamic mode setup. Fig. S2. Reconstruction of the graphite particles in the water phase. Fig S3. Holographic reconstruction of graphite solid particles. Fig. S4. Reconstruction of the intensity information for BC particles in the solid phase. Fig. S5. Holographic reconstruction of single walled carbon nanotube solid particles CNT. Fig. S6. Holographic reconstruction of single walled carbon nanotube solid particle agglomerates. And Table S1: Different aerosol characterization methods with their advantages and limitations. See DOI: **https://doi.org/10.1039/d5ra03401a**.

Acknowledgements

References

1 Y. J. Kaufman and O. Boucher, *Facing Climate Change Together*, 2008, pp. 49–61.

2 U. Pöschl, *Angew. Chem., Int. Ed.*, 2005, **44**, 7520–7540.

3 Z. J. Wu, J. Chen, Y. Wang, Y. S. Zhu, Y. C. Liu, B. Yao, Y. H. Zhang and M. Hu, *Natl. Sci. Rev.*, 2018, **5**, 452–454.

4 M. Kanakidou, J. H. Seinfeld, S. N. Pandis, I. Barnes, F. J. Dentener, M. C. Facchini, R. Van Dingenen, B. Ervens, A. Nenes, C. J. Nielsen, E. Swietlicki, J. P. Putaud, Y. Balkanski, S. Fuzzi, J. Horth, G. K. Moortgat, R. Winterhalter, C. E. L. Myhre, K. Tsigaridis, E. Vignati, E. G. Stephanou and J. Wilson, *Atmos. Chem. Phys.*, 2005, **5**, 1053–1123.

5 T. C. Bond, S. J. Doherty, D. W. Fahey, P. M. Forster, T. Berntsen, B. J. DeAngelo, M. G. Flanner, S. Ghan, B. Kärcher, D. Koch, S. Kinne, Y. Kondo, P. K. Quinn, M. C. Sarofim, M. G. Schultz, M. Schulz, C. Venkataraman, H. Zhang, S. Zhang, N. Bellouin, S. K. Guttikunda, P. K. Hopke, M. Z. Jacobson, J. W. Kaiser, Z. Klimont, U. Lohmann, J. P. Schwarz, D. Shindell, T. Storelvmo, S. G. Warren and C. S. Zender, *J. Geophys. Res. Atmos.*, 2013, **118**, 5380–5552.

6 A. Laskin, J. Laskin and S. A. Nizkorodov, *Chem. Rev.*, 2015, **115**, 4335–4382.

7 D. Koch, S. Menon, A. Del Genio, R. Ruedy, I. Alienov and G. A. Schmidt, *J. Climatol.*, 2009, **22**, 2659–2677.

8 X. Wang, X. Luo, Y. Zhang, S. Kang, P. Chen and H. Niu, *Environ. Sci. Pollut. Res. Int.*, 2024, **31**, 3413–3424.

9 A. K. Mishra, I. Koren and Y. Rudich, *Heliyon*, 2015, **1**(2), e00036.

10 C. Di Biagio, A. di Sarra, P. Eriksen, S. E. Ascanius, G. Muscari and B. Holben, *Clim. Dyn.*, 2012, **39**, 953–969.

11 M. J. Heavner, D. A. Smith, A. R. Jacobson and R. J. Sheldon, *J. Geophys. Res. Atmos.*, 2002, **107**(D24), ACL 19-1.

12 C. Carbone, S. Decesari, M. Mircea, L. Giulianelli, E. Finessi, M. Rinaldi, S. Fuzzi, A. Marinoni, R. Duchi, C. Perrino, T. Sargolini, M. Vardè, F. Sprovieri, G. P. Gobbi, F. Angelini and M. C. Facchini, *Atmos. Environ.*, 2010, **44**, 5269–5278.

13 M. Z. Jacobson, *J. Geophys. Res. Atmos.*, 2014, **119**, 8980–9002.

14 D. Koch and A. D. Del Genio, *Atmos. Chem. Phys.*, 2010, **10**, 7685–7696.

15 P. J. DeMott, Y. Chen, S. M. Kreidenweis, D. C. Rogers and D. E. Sherman, *Geophys. Res. Lett.*, 1999, **26**, 2429–2432.

16 B. T. Johnson, J. M. Haywood and M. K. Hawcroft, *J. Geophys. Res. Atmos.*, 2019, **124**, 7930–7950.

17 C. A. Gueymard, V. Lara-Fanego, M. Sengupta and Y. Xie, *Sol. Energy*, 2019, **182**, 194–212.

18 Y. Liu, J. H. Huang and F. Huang, *IEEE Access*, 2023, **11**, 36763–36786.

19 Y. Zhang, O. Favez, F. Canonaco, D. Liu, G. Močnik, T. Amodeo and A. Albinet, *npj Clim. Atmos. Sci.*, 2018, **1**(1), 47.

20 A. Laskin, R. C. Moffet and M. K. Gilles, *Acc. Chem. Res.*, 2019, **52**, 3419–3431.

21 Z. He, K. Liu and J. Wang, *Acc. Chem. Res.*, 2018, **51**, 1082–1091.

22 D. Pal, Y. Nazarenko, T. C. Preston and P. A. Ariya, *Commun. Chem.*, 2021, **4**(1), 170.

23 V. Harik, *Trends in Nanoscale Mechanics: Mechanics of Carbon Nanotubes, Graphene, Nanocomposites and Molecular Dynamics*, 2014, pp. 197–211.

24 S. Fiedler, V. Naik, F. M. O'Connor, C. J. Smith, P. Griffiths, R. J. Kramer, T. Takemura, R. J. Allen, U. Im, M. Kasoar, A. Modak, S. Turnock, A. Voulgarakis, D. Watson-Parris, D. M. Westervelt, L. J. Wilcox, A. L. D. Zhao, W. J. Collins, M. Schulz, G. Myhre and P. M. Forster, *Geosci. Model Dev.*, 2024, **17**, 2387–2417.

25 T. C. a. C. A. C. (CCAC), *Black Carbon: An air pollutant with damaging effects on human health, crops, ecosystems and climate*, 2024, **https://www.ccacoalition.org/short-lived-climate-pollutants/black-carbon#sources**.

26 N. A. Janssen and WHO, *Health Effects of Black Carbon*, WHO Regional Office for Europe, Copenhagen, 2012, vol. 41.

27 D. Pal, *Doctor of Philosophy P.h.D Manuscript*, McGill University, 2023.

28 P. H. McMurry, *Atmos. Environ.*, 2000, **34**, 1959–1999.

29 T. M. Kreis, M. Adams and W. P. O. Juptner, *Proc. Soc. Photo Opt. Instrum. Eng.*, 1997, **3098**, 224–233.

30 H. J. Li and P. A. Ariya, *J. Geophys. Res. Atmos.*, 2021, **126**(22), e2021JD035265.

31 T. Klein, E. Buhr and C. G. Frase, *Adv. Imag. Electron. Phys.*, 2012, **171**, 297–356.

32 G. A. Zheng, C. Shen, S. W. Jiang, P. M. Song and C. H. E. Yang, *Nat. Rev. Phys.*, 2021, **3**, 207–223.

33 B. Bazow, T. Phan, C. B. Raub and G. Nehmetallah, *Opt. Express*, 2023, **31**, 28382–28399.

34 R. K. Chakrabarty, N. D. Beres, H. Moosmüller, S. China, C. Mazzoleni, M. K. Dubey, L. Liu and M. I. Mishchenko, *Sci. Rep.*, 2014, **4**(1), 5508.

35 T. C. Bond and R. W. Bergstrom, *Aerosol Sci. Technol.*, 2006, **40**, 27–67.

36 Z. Wang, A. Pilechi, M. F. Cheung and P. A. Ariya, *Water Res.*, 2023, **235**, 119898.

37 R. Hall, D. Pal and P. A. Ariya, *Anal. Chem.*, 2022, **94**, 11390–11400.

38 J. Garcia-Sucerquia, W. B. Xu, S. K. Jericho, P. Klages, M. H. Jericho and H. J. Kreuzer, *Appl. Opt.*, 2006, **45**, 836–850.

39 S. K. Jericho, P. Klages, J. Nadeau, E. M. Dumas, M. H. Jericho and H. J. Kreuzer, *Planet. Space Sci.*, 2010, **58**, 701–705.

40 T. R. Liu, Z. S. Wei, Y. Rivenson, K. de Haan, Y. B. Zhang, Y. C. Wu and A. Ozcan, *J. Biophot.*, 2019, **12**(11), e201900107.

41 Z. Wang, D. Pal, A. Pilechi and P. A. Ariya, *Environ. Sci. Technol.*, 2024, **58**, 8919–8931.

42 D. Pal, M. Amyot, C. Liang and P. A. Ariya, *Commun. Eng.*, 2023, **2**(1), 41.

43 D. Litwiller, *Photon. Spectra.*, 2005, **39**, 54.

44 S. G. Aggarwal, *MAPAN-J. Metrol. Soc. India*, 2010, **25**, 165–189.

45 M. Yamada, M. Takaya and I. Ogura, *Ind. Health*, 2015, **53**, 511–516.

46 J. Lee, D. Yoo, S. Ryu, S. Ham, K. Lee, M. Yeo, K. Min and C. Yoon, *Aerosol Air Qual. Res.*, 2019, **19**, 840–853.

47 D. Pal, A. Dastoor and P. A. Ariya, *Urban Clim.*, 2020, **34**, 100713.

48 M. Rahim, D. Pal and P. Ariya, *Environ. Pollut.*, 2018, **246**, 734–744.

49 J. Kasparian, C. Hassler, B. Ibelings, N. Berti, S. Bigorre, V. Djambazova, E. Gascon-Diez, G. Giuliani, R. Houlmann, D. Kiselev, P. de Laborie, A. D. Le, T. Magouroux, T. Neri, D. Palomino, S. Pfandler, N. Ray, G. Sousa, D. Staedler, F. Tettamanti, J. P. Wolf and M. Beniston, *Sci. Rep.*, 2017, **7**, 45476.

50 W. Xu, M. H. Jericho, I. A. Meinertzhagen and H. J. Kreuzer, *Appl. Opt.*, 2002, **41**, 5367–5375.

51 L. Dixon, F. C. Cheong and D. G. Grier, *Opt. Express*, 2011, **19**, 16410–16417.

52 A. L. Bondy, D. Bonanno, R. C. Moffet, B. B. Wang, A. Laskin and A. P. Ault, *Atmos. Chem. Phys.*, 2018, **18**, 12595–12612.

53 C. M. Long, M. A. Nascarella and P. A. Valberg, *Environ. Pollut.*, 2013, **181**, 271–286.

54 R. A. Forrest, H. Marsh, C. Cornford and B. T. Kelly, *In Chemistry & Physics of Carbon*, CRC Press, 2021, pp. 211–330.

55 O. L. Hadley and T. W. Kirchstetter, *Nat. Clim. Change*, 2012, **2**(6), 437–440.

56 W. C. Hinds and Y. Zhu, *Aerosol Technology: Properties, Behavior, and Measurement of Airborne Particles*, John Wiley & Sons, 2022.

57 M. G. Flanner, X. Liu, C. Zhou, J. E. Penner and C. Jiao, *Atmos. Chem. Phys.*, 2012, **12**(10), 4699–4721.

58 D. Pal, R. Hall, Y. Nazarenko, L. Barrie and P. A. Ariya, *npj Clim. Atmos. Sci.*, 2025, **8**(1), 204.

59 A. M. Dimiev, K. Shukhina, N. Behabtu, M. Pasquali and J. M. Tour, *J. Phys. Chem. C*, 2019, **123**, 19246–19253.

60 C. Jiang, S. Liu, T. Zhang, Q. Liu, P. J. J. Alvarez and W. Chen, *Environ. Sci. Technol.*, 2022, **56**, 7426–7447.

61 J. Garcia-Sucerquia, W. Xu, S. K. Jericho, P. Klages, M. H. Jericho and H. J. Kreuzer, *Appl. Opt.*, 2006, **45**, 836–850.

62 M. O. Andreae and A. Gelencsér, *Atmos. Chem. Phys.*, 2006, **6**(10), 3131–3148.